Viscous Acceleration Vector Field as a Tool for the Analysis of Vortical Structures

Ondřej Urban[1,2], František Pochylý[1], Jakub Šístek[3], Marek Pátý[3,4], David Štefan[a),1]

[1] Brno University of Technology, Faculty of Mechanical Engineering, Energy Institute, Viktor Kaplan Department of Fluid Engineering, Technická 2896/2, 616 69 Brno, Czech Republic

[2] Litostroj Engineering a.s., Technická 3029/17, 616 00 Brno, Czech Republic

[3] Institute of Mathematics of the Czech Academy of Sciences, Žitná 25, 115 67 Prague, Czech Republic

[4] Czech Technical University in Prague, Technická 4, 166 00 Prague, Czech Republic

[a)] Author to whom correspondence should be addressed: David.Stefan@vut.cz

Abstract. This paper demonstrates how the viscous acceleration vector field can be used in the study of vortical structures and, more generally, in flow topology analysis. First, the problem of frame dependence in vortex identification and flow topology analysis is revisited. The viscous acceleration vector field is then introduced as a suitable objective quantity, being independent of both frame translation and rotation. We propose several innovative approaches based on it. Following an idea from the literature of treating the viscous acceleration field as a pseudo-velocity field, we show that its integral curves (or streamlines) can be utilized for flow topology analysis. Thanks to the objectivity, they reveal structures that may be hidden in frame-dependent velocity representations. To support this framework, we employ a less widely recognized Eulerian definition of streamline curvature and torsion. Further, we show that the Eulerian representation of the curvature of viscous acceleration field lines can be used in connection with a vortex identification method (in this case residual vorticity) to obtain enhanced visualizations of vortical structures through volume rendering. The proposed methods are tested on three distinct cases of computational fluid dynamics (CFD) simulations, ranging from laminar flow to fully-resolved turbulent flow. The results support their applicability in the post-processing of CFD data.

Nomenclature

a_i	Acceleration caused by external forces (m·s^{-2})	t_i, $\boldsymbol{t}$	Unit tangent vector (1)
$\boldsymbol{a}_\mu$	Viscous acceleration vector (m·s^{-2})	v_i, $\boldsymbol{v}$	Velocity vector (m·s^{-1})
b_i, $\boldsymbol{b}$	Unit binormal vector (1)	$\tilde{v}_i$, $\tilde{\boldsymbol{v}}$	Pseudo-velocity vector (m^{-1}·s^{-1})
CFD	Computational fluid dynamics	V_{ij}	Velocity gradient tensor (s^{-1})
DNS	Direct numerical simulation	x, y, z	Cartesian coordinates (m)
H	Heaviside function	x_i, $\boldsymbol{x}$	Vector of Cartesian coordinates (m)
I	Invariants of a tensor	δ_{ij}	Kronecker delta
LES	Large eddy simulation	ε_{ijk}	Levi-Civita symbol
LIC	Line integral convolution	κ	Streamline curvature (m^{-1})
n_i, $\boldsymbol{n}$	Unit normal vector (1)	λ	Volume viscosity (Pa·s), eigenvalue

p	Pressure (Pa)	λ_ω	λ_ω-criterion (m^{-1}·s^{-1})
PIV	Particle image velocimetry	μ	Dynamic viscosity (Pa·s)
r, φ, z	Cylindrical coordinates (m, 1, m)	ρ	Density (kg·m^{-3})
Q	Q-criterion (s^{-2})	τ	Streamline torsion (m^{-1})
RANS	Reynolds-averaged Navier−Stokes equations	φ_i	Eigenvector
Re	Reynolds number (1)	ω_i, $\boldsymbol{\omega}$	Vorticity (s^{-1})
S_{ij}, $\boldsymbol{S}$	Strain-rate tensor (s^{-1})	$\tilde{\omega}_i$, $\tilde{\boldsymbol{\omega}}$	Pseudo-vorticity vector (m^{-2}·s^{-1})
SBES	Stress-blended eddy simulation	$\boldsymbol{\omega}_{\mathrm{res}}$	Residual vorticity vector (s^{-1})
t	Time (s)	$\boldsymbol{\Omega}$, Ω_{ij}	Vorticity tensor (s^{-1})

I. INTRODUCTION

It was Leonardo da Vinci in the early 16th century who first made scientific observations of vortical structures. Thanks to his artistic skills, he was able to create detailed sketches of various flow phenomena [1]. He was ahead of his time – similar experiments by Reynolds and the discovery of the governing equations did not come until more than three centuries later. Many notable scientists then described specific cases of vortical structures, e.g., von Kármán vortex street behind blunt bodies, Taylor vortices in the gap between two rotating cylinders, or Kelvin–Helmholtz vortices as a result of shear layer instability [2].

The knowledge of the mentioned and other vortical structures is important in practice, both in terms of exploiting them in industrial technologies as well as avoiding undesirable effects, e.g., in off-design conditions in turbomachinery. Yet, the question of how to correctly identify vortical and other structures in flow remains open, particularly due to the frame dependence of the velocity field. This excludes velocity streamlines, otherwise a common tool for flow visualization, from being used for vortex identification and flow topology studies in unsteady flows. Majority of existing works are therefore focused on the Galilean-invariant velocity gradient tensor. These include the Q-criterion [3], the λ_2-criterion [4], swirling strength [5], residual vorticity [6], or Rortex [7]. For more comprehensive reviews, see [6, 8, 9].

In this paper, we propose to use the viscous acceleration vector field as a tool for the analysis of vortical structures. This dynamic quantity is objective (independent of both frame translation and rotation) and originates from the relative motion of fluid particles. It has a non-zero magnitude if the local velocity differs from the local average velocity; that is, when the velocity profile is nonlinear. The connection with shearing and straining motion of fluid particles, which is directly related to the relative velocity pattern, makes the viscous acceleration vector field relevant for flow topology studies. Consider, for example, a simple steady vortex with a nonlinear velocity profile, e.g. a Lamb vortex. In this case, the viscous acceleration field is exactly tangent to the velocity field and its field lines form closed loops. In contrast, pressure acceleration, which is also objective, points towards the votrex center. The corresponding centripetal force bends the trajectory of fluid particles. Our assumption for vortex identification therefore is that in vortices, viscous acceleration vector field lines form closed loops or spiral shapes. Calculation of these lines is easy and fast in common post-processing software.

We also define a combination of the Eulerian representation of the curvature of viscous acceleration vector field lines with a vortex criterion to obtain enhanced visualizations of vortical structures in various cases of CFD simulations. We note that analysis of possible errors in the test data generated by numerical schemes is outside our current scope. These include spurious vortices as discussed in [10] or the effect of numerical-physical coupling on the captured structures in scale-resolving turbulent flow simulations [11]. We justify this decision by the fact that methods for vortex identification and flow topology analysis must work for any velocity field, whether realistic or not. Our goal is to be able to identify all well-resolved structures with respect to the grid size, i.e., not noisy ones.

First, a brief overview of the state of the art in vortex identification with a description of chosen methods is given in Section II. Then, possible adjustments of a velocity field to achieve at least Galilean invariance are described in Section III. Viscous acceleration field and its properties are discussed in

Section IV. The Eulerian expressions of streamline curvature and torsion, which will be subsequently applied to the viscous acceleration vector field, are presented in Section V. Finally, practical applications are the subject of Section VI.

II. STATE OF THE ART IN VORTEX IDENTIFICATION

A necessary prerequisite for being able to talk about vortical structures is the ability to define them. Although the notion of vortical structures as regions in a fluid characterized by orbiting of particles around a center line may seem simple, finding a precise definition and identification method has turned out to be challenging, and there is still no universally-accepted definition of a vortex. For example, Kolář [6], Epps [8], and Chakraborty et al. [9] discussed this problem in their papers. We provide here some of the considerations in order to bring insight into the difficulties involved.

Throughout this work, we employ Einstein notation (index notation, where repeated indices within a term imply summation) alongside matrix notation. In the latter, scalars are denoted by lightface letters, vectors and matrices by boldface letters, and operations by standard operators such as div, curl or ∇. This is because both ways have their own advantages and disadvantages. For some expressions, one is preferable, while for others, the other is more suitable.

The vorticity vector defined as

$$\omega_i = \varepsilon_{ijk}\frac{\partial v_k}{\partial x_j} = \operatorname{curl}\boldsymbol{v} \tag{1}$$

may seem to be a suitable candidate for vortex identification as it is a measure of the rotation of fluid particles – vorticity magnitude is twice the angular velocity of the particle. However, particles rotate also in shearing layers, leading to nonzero vorticity therein. Moreover, vorticity in viscous flows is diffused, meaning that there is no sharp boundary between rotational and irrotational flow. Another option might seem to be finding closed or spiral streamlines, but this works only in steady flow. Vortices can be transported by external flow, which also affects the streamline pattern. Therefore, the velocity gradient tensor is used in many methods, some of which will be introduced later in this section. These methods are Galilean-invariant, i.e., independent of frame translation. However, a proper vortex identification method should be objective – independent also of frame rotation. An example of such a method is the M_Z-criterion introduced by Haller [12]. It is based on an analysis of the pathlines of fluid particles but is applicable only to incompressible flow. In the following, we will introduce the theory behind some methods based on the velocity gradient tensor.

Several vortex identification methods based on the velocity gradient tensor were derived from its eigenvalues. The velocity gradient tensor is defined and decomposed as

$$V_{ij} = \frac{\partial v_i}{\partial x_j} = \frac{1}{2}\left(\frac{\partial v_i}{\partial x_j} + \frac{\partial v_j}{\partial x_i}\right) + \frac{1}{2}\left(\frac{\partial v_i}{\partial x_j} - \frac{\partial v_j}{\partial x_i}\right) = S_{ij} + \Omega_{ij} \tag{2}$$

where the symmetric part S_{ij} is called the strain-rate tensor, and the skew-symmetric part Ω_{ij} is called the vorticity tensor, as its non-zero elements correspond to the vorticity elements ω_i. The eigenvalue problem is given by the following equation

$$\left(V_{ij} - \lambda\delta_{ij}\right)\varphi_j = 0 \tag{3}$$

where λ is an eigenvalue, δ_{ij} the Kronecker delta, and φ_j an eigenvector. This equation has a nonzero solution only if $\det\left(V_{ij} - \lambda\delta_{ij}\right) = 0$, leading to the following characteristic equation

$$\lambda^3 - I_1\lambda^2 + I_2\lambda - I_3 = 0 \tag{4}$$

where I_i is the i-th invariant of the velocity gradient tensor. These invariants do not depend on the reference frame origin and orientation, and they are defined as

$$\begin{gathered} I_1 = \operatorname{div} \boldsymbol{v} = -P = \lambda_1 + \lambda_2 + \lambda_3 \\ I_2 = \frac{1}{2}(\operatorname{tr}\nabla\boldsymbol{v})^2 - \frac{1}{2}\operatorname{tr}(\nabla\boldsymbol{v})^2 = Q = \lambda_1\lambda_2 + \lambda_1\lambda_3 + \lambda_2\lambda_3 \\ I_3 = \det\nabla\boldsymbol{v} = -R = \lambda_1\lambda_2\lambda_3 \end{gathered} \tag{5}$$

These relations have given rise to several vortex identification methods. The widely used Q-criterion, introduced for incompressible fluids by Hunt et al. [3], defines vortices as regions with a positive value of Q, which can be written as

$$Q = \frac{1}{2}(\operatorname{tr}\nabla\boldsymbol{v})^2 + \frac{1}{2}(\|\boldsymbol{\Omega}\|^2 - \|\mathbf{S}\|^2) = \frac{1}{2}\left(\frac{\partial v_i}{\partial x_i}\frac{\partial v_j}{\partial x_j} - \frac{\partial v_i}{\partial x_j}\frac{\partial v_j}{\partial x_i}\right) \tag{6}$$

For incompressible fluids, where the first term is zero, this physically means that vortices are regions where vorticity dominates over the strain rate in terms of their norms. For compressible flow, the Q-criterion is dubious, as it allows positive values in regions with no vorticity but high compression or expansion [8].

Several other methods assume that, within vortices, two of the three eigenvalues form a complex conjugate pair. This happens if the streamline pattern obtained after the local velocity subtraction is closed or spiral. The discriminant of the characteristic equation (4) is negative, i.e., for incompressible flows

$$D = -108\Delta = -4{I_2}^3 - 27{I_3}^2 = -4Q^3 - 27R^2 < 0 \tag{7}$$

This Δ-criterion [13] is clearly less restrictive than the Q-criterion. The swirling strength criterion by Zhou et al. [5] exploits the same definition for the determination of vortex regions, and it uses the imaginary part of the complex eigenvalues as a measure of their strength. The Rortex (a.k.a. Liutex) [7] further equips the method with a vectorial nature, employing the direction of the eigenvector corresponding to the real eigenvalue. One serious flaw of the methods based on imaginary eigenvalues of the velocity gradient tensor is the so-called disappearing vortex problem. Loosely speaking, the issue lies in the fact that, for certain flows with fixed topology but varying vorticity magnitude, the outcome—whether the flow is classified as a vortex—can differ [9, 14].

An interesting vortex identification method, which will be used in this study, is based on the triple decomposition of the velocity gradient tensor by Kolář [6]. Unlike the standard double decomposition (2), the velocity gradient is decomposed into the "effective" pure shear part and the residual part, which is further decomposed into the residual strain rate (describing irrotational straining motion) and the residual vorticity (describing rigid-body rotation)

$$\nabla\boldsymbol{v} = \nabla\boldsymbol{v}_{\text{shear}} + \nabla\boldsymbol{v}_{\text{residual}} = \nabla\boldsymbol{v}_{\text{shear}} + \mathbf{S}_{\text{residual}} + \boldsymbol{\Omega}_{\text{residual}} \tag{8}$$

The residual vorticity vector, which is extracted from $\boldsymbol{\Omega}_{\text{residual}}$, is then used for vortex identification.

The triple decomposition procedure starts with finding the so-called basic reference frame, where the effect of shear extraction is maximized. The following relation for the norm of the residual part can be derived:

$$\|\nabla\boldsymbol{v}_{\text{residual}}\|^2 + 4(|S_{12}\Omega_{12}| + |S_{23}\Omega_{23}| + S_{31}\Omega_{31}) = \|\nabla\boldsymbol{v}\|^2 \tag{9}$$

To minimize the norm of the residual part, we have to find such orientation of the reference frame, where the second term is maximized. This task has to be in three-dimensional space solved iteratively using a suitable optimization algorithm. Solving this optimization problem for every spatial point presents a significant computational burden, which is the main drawback of this method. For meshes in the order of millions of points, using a regular personal computer, processing a single snapshot may take several minutes. In this work, we start with a regular grid of points representing rotation angles covering the definition space. After identification of the best point from this grid, we refined the results using the gradient descent.

Once the basic reference frame is found, the residual part of the velocity gradient tensor is extracted as follows

$$\nabla v_{\mathrm{residual}_{ij}} = \mathrm{sgn}\left(\frac{\partial v_i}{\partial x_j}\right) \min\left(\left|\frac{\partial v_i}{\partial x_j}\right|, \left|\frac{\partial v_j}{\partial x_i}\right|\right) \tag{10}$$

Finally, the residual vorticity in the basic reference frame is extracted from the antisymmetric part of $\nabla \boldsymbol{v}_{\mathrm{residual}}$ and rotated back to the original reference frame. It represents the portion of the total vorticity that is not associated with shear motion. Unlike the previously mentioned methods, due to its vectorial nature, it also indicates the vortex orientation. Its magnitude can be used as a measure of the vortex strength, and it represents twice the angular velocity of the underlying rotation, just like the regular vorticity. Readers interested in a step-by-step description of the calculation algorithm used in this study are referred to [15]. Practical applications of this method can be found in [16, 17].

III. TOWARDS OBJECTIVE VECTOR FIELDS

The fact that the observed fluid velocity depends on the velocity of the coordinate frame hinders vortex identification and, more generally, flow topology analysis. If the flow patterns are transported either by a free stream or by the coordinate frame motion, the streamline patterns are affected by the transport velocity. Common pointwise methods therefore rely on subtracting the local velocity, leading to zero velocity in the point of interest (critical point) and a flow pattern in its vicinity [18, 19].

To illustrate the problem, we consider flow around a circular cylinder at $\mathrm{Re} = 100$. Figure 1 shows contours of an instantaneous velocity magnitude field and an LIC (Line Integral Convolution) texture revealing the streamline pattern for two reference frames. The first is the original reference frame, in which the cylinder is steady and the fluid flows around it. The second is a relative reference frame moving at the fluid inflow velocity. Both these reference frames are inertial; that is, the velocity field together with the pressure field satisfy the Navier–Stokes equation (11). Although the dynamics are the same, the velocity field topology is very different.

The original frame reveals one vortex in the cylinder wake. Its center is a critical point – the velocity is zero. The only other critical point is located on the front side of the cylinder. At this point, the flow bifurcates to the left and right side. The flow pattern downstream of the cylinder is wavy and consists of alternating zones of lower and higher velocities. In contrast, the flow pattern downstream of the cylinder in the relative frame consists of a row of vortices, the so-called von Kármán vortex street. These vortices detach from the cylinder and they are transported downstream at the inflow velocity. Subtracting the inflow velocity from the original velocity field reveals them. A saddle point can be seen on that side of each vortex where the velocity direction does not match the direction of the surrounding flow. To see all relevant structures in one picture, it is therefore desirable to find an invariant velocity field that retains the topological characteristics, i.e., closed or spiral streamlines in vortical structures, important critical points, saddles, sources and sinks for compressible flow, etc., and eliminates the pure transport velocity from instantaneous velocity fields.

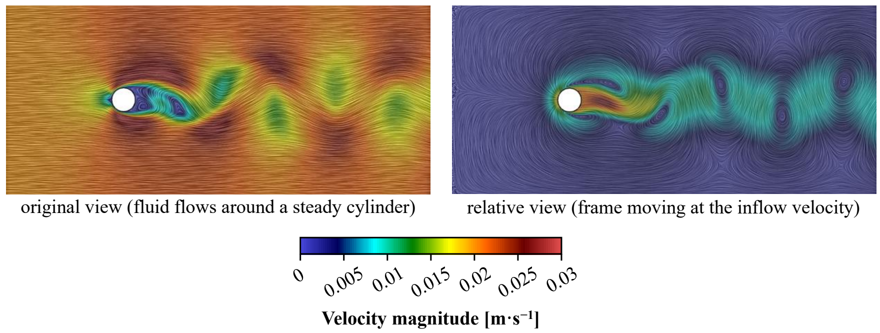

Figure 1. Velocity field of flow around a circular cylinder at $\mathrm{Re} = 100$ – contours of velocity magnitude and LIC texture visualizing the streamline pattern. The cylinder diameter is $D = 5$ mm, the inflow velocity is $v_\infty = 0.02$ m·s^{-1}, and the fluid viscosity is $\nu = 1.003 \cdot 10^{-6}$ m^2·s^{-1}. A uniform inflow velocity profile, frictionless side walls and a constant static pressure at the outlet were considered.

The problem of finding a suitable invariant velocity field for studying flow topology is the subject of research efforts. Often, the steady solution or a time-averaged velocity field is subtracted from instantaneous velocity fields to study fluctuations. This approach, in principle, removes steady structures. To preserve them, more sophisticated methods need to be applied.

The Helmholtz-Hodge decomposition theorem states that vector fields can be decomposed into divergence-free and rotation-free components [20]. The rotation-free component has a scalar potential; therefore, the potential flow theory applies. This inspired Wiebel et al. [21] to calculate the potential flow induced by the original boundary conditions and subtract it from the original velocity field. Since the potential flow responds to the frame translation in the same manner as the original flow, the resulting localized flow is Galilean-invariant. Furthermore, since potential flow is generally curl-free, the vorticity of the localized flow remains identical to the original flow.

Günther et al. [22] introduced an objective (independent of both translation and rotation of the reference frame) velocity field obtained by minimizing unsteadiness in a chosen area around a point of interest. In other words, the goal is to find such a moving reference frame, in which the integral of the unsteadiness of the flow is minimized. The results depend on the size and shape of the chosen area; the recommended size should be comparable to the flow structures of interest. The authors later generalized the method for any smooth similarity transformation and any smooth affine transformation of the reference frame [23].

Fig. 2 shows the abovementioned velocity fields for the case of flow around a circular cylinder. The potential flow subtraction led to results similar to the relative view in Fig. 1. The main differences are located close to the cylinder. For the method of Günther et al., only an LIC texture is shown. The velocity magnitude field is not meaningful in this case. With both methods, we can identify all the vortices, but their shape and center position differ. For the sake of comparison, vortex centers defined as the local maxima of the residual vorticity magnitude and by the method of Wiebel et al. as the centers of closed streamlines are marked with crosses. The locations of vortex centers are generally different among the methods, with the differences being most significant close to the cylinder. This illustrates the difficulty of finding the correct vortex centers. Just as in general vortex identification, different methods of vortex center identification were formulated and published in literature [24–27].

One serious disatvantage of the objective velocity field by Günther et al. is, again, the prohibitive computational cost required to obtain it. Therefore, we see cheaply-calculated viscous acceleration as a suitable alternative.

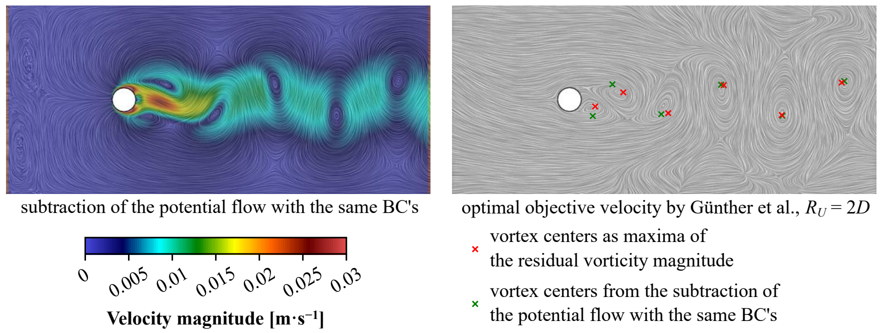

Figure 2. Two velocity fields for the same case as in Fig. 1. Left: localized flow obtained by subtracting the potential flow with the same inlet velocity as the original flow as suggested by Wiebel et al. [21] (Galilean-invariant velocity field). Right: LIC texture of the optimal velocity field by Günther et al. [22] as observed locally from the reference frame that minimizes the observed unsteadiness in neighborhood with radius $R_U = 2D$, where D is the cylinder diameter (objective velocity field). Vortex cores obtained as maxima of the residual vorticity magnitude and as the centers of closed streamlines by the method of Wiebel et al. are included, marked with crosses.

IV. VISCOUS ACCELERATION

The previous section illustrated the ambiguity of finding an invariant velocity field suitable for studying flow structures. Despite this, kinematic quantities derived from the velocity field and its gradient tensor tend to be preferred over dynamic quantities. The latter are included in the Navier–Stokes equation, which, for an incompressible Newtonian fluid, reads

$$\frac{\partial v_i}{\partial t} + \frac{\partial v_i}{\partial x_j} v_j = a_i - \frac{1}{\rho}\frac{\partial p}{\partial x_i} + \frac{\mu}{\rho}\frac{\partial^2 v_i}{\partial x_j \partial x_j} \tag{11}$$

Relevant dynamic quantities are the particle acceleration, pressure acceleration, and viscous acceleration. The particle acceleration (left-hand side) must be defined in an inertial reference frame. If the reference frame is non-inertial (i.e., accelerating), fictitious forces have to be included (e.g., centrifugal and Coriolis force for rotating reference frames). Importantly, for this paper, pressure and viscous acceleration are objective. Pressure acceleration is caused by pressure gradients, which, in a real fluid, originate from collisions of microscopic fluid particles. In vortices, this provides the centripetal acceleration required for the curved motion of macroscopic fluid elements around a vortex core. Viscous acceleration, on the other hand, arises from viscous stress, which is present only when relative motion between fluid particles exists. The orientation of viscous forces corresponds to the direction along which fluid momentum is diffused, resulting in the dissipation of mechanical energy into heat. In vortices, if not compensated, this causes a decay in rotational speed (the tangential component) or a deformation of the vortex shape (the normal component). This sensitivity to the local velocity structure makes the viscous acceleration field a well-suited candidate for characterizing the flow topology.

The fluid viscosity is included in the Reynolds number, the quantity allowing us to distinguish between different flow regimes (particularly laminar and turbulent flow). Similar to streamlines for the velocity field, it is possible to construct lines tangent to the viscous acceleration vectors. These lines are generally called vector field lines. For laminar flow, these lines define the layers that gave laminar flow its name.

The viscous acceleration is, for an incompressible Newtonian fluid, defined as

$$\boldsymbol{a}_{\mu} = \frac{\mu}{\rho}\Delta\boldsymbol{v} = \frac{\mu}{\rho}\frac{\partial^2 v_i}{\partial x_j \partial x_j} \tag{12}$$

With the velocity field available, its calculation is straightforward and fast compared to objective velocity fields, which typically require time-consuming operations. A disadvantage is the presence of the second spatial derivative, as its numerical estimation is often prone to discretization errors and noise amplification. We note that viscosity applies even if the viscous acceleration is zero. This occurs in linear relative velocity profiles, where viscous forces acting on the opposite sides of an elementary volume cancel out (having the same magnitude but opposite directions). This is the case in the Couette flow. In Fig. 3, which shows the viscous acceleration field for our case of flow around a cylinder, the entire von Kármán vortex street is clearly visible. Vortex centers, determined as the centers of closed field lines, correspond closely to those obtained by the method of Günther et al.

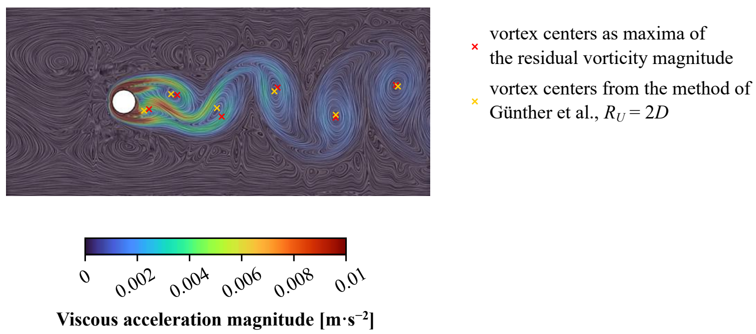

Figure 3. Viscous acceleration field (LIC texture and contours of magnitude) for the same case as in Figs. 1 and 2. Vortex cores obtained as maxima of the residual vorticity magnitude and as the centers of closed streamlines from the method of Günther et al. are included, marked with crosses.

To better understand how viscous acceleration behaves, we consider a superposition of two flows – a Lamb vortex and pure shear. The Lamb vortex is defined in cylindrical coordinates and has the form $\boldsymbol{v}_{\mathrm{v}}{}^{\mathrm{T}} = \left(0, v_{\varphi}, 0\right)$, where

$$v_{\varphi}(r) = \frac{\Gamma}{2\pi r}\left(1 - \mathrm{e}^{-\frac{r^2}{t}}\right) \tag{13}$$

In this case, we chose $\Gamma = 1$, $t = 0.04$. The pure shear component is defined in Cartesian coordinates and has the form $\boldsymbol{v}_{\mathrm{s}}{}^{\mathrm{T}} = (1 - y^2, 0,0)$. The resulting flow is defined as

$$\boldsymbol{v} = \boldsymbol{v}_{\mathrm{v}} + k_{\mathrm{s}}\boldsymbol{v}_{\mathrm{s}} \tag{14}$$

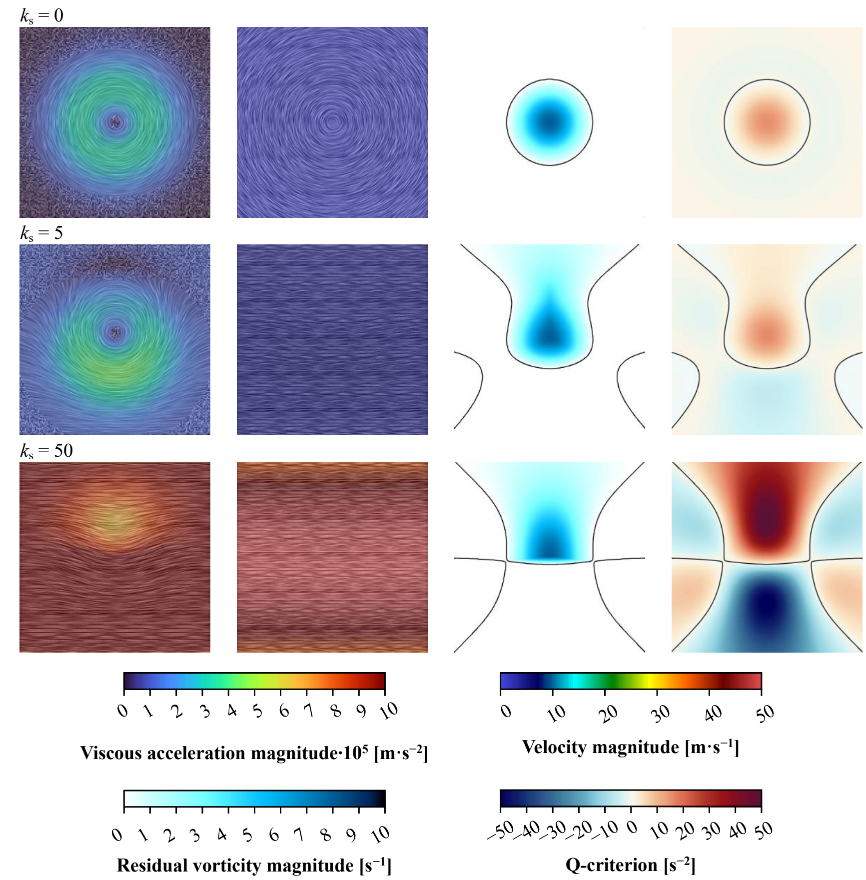

Figure 4. Superposition of a Lamb vortex and pure shear defined by equation (14) for three intensities of the shear component k_s (from top to bottom). From left: viscous acceleration field (contours of magnitude and LIC texture), velocity field (contours of magnitude and LIC texture), residual vorticity magnitude with zero isoline, and the Q-criterion with zero isoline.

Figure 4 shows the viscous acceleration field, velocity field, and chosen vortex criteria (residual vorticity and the Q-criterion) for three values of k_s (the shear component intensity). Vortices are in the last two columns manifested by positive values. For $k_s = 0$, we have only the Lamb vortex, which the criteria identify correctly. The viscous acceleration field is parallel to the velocity field, and the vortex center is clearly visible. This indicates that viscous forces in this case act merely as tangential friction. The centripetal force, which is necessary for sustained orbiting, is provided by the pressure force. Noisy texture appears in the outer zone, where the viscous acceleration magnitude becomes negligible, making the LIC calculation unstable. Increasing k_s to 5 (in the second row) decreases the viscous acceleration in the upper half and increases it in the lower half. Its vector field lines are still closed in a certain zone, unlike velocity streamlines, which are almost straight. The center of the vortex is shifted up compared to the previous case. The vortex criteria correspondingly indicate a vortex in the upper half, with the peak value point corresponding to the center of the viscous acceleration lines. Increasing k_{s} to 50 (in the last row) eliminates closed viscous acceleration vector field lines. However, the vortex criteria still indicate vortex regions. Moreover, the peak values of the Q-criterion are higher than in the previous cases, suggesting that the alleged vortices are even stronger. The shear elimination procedure in the residual vorticity definition at least prevents this increase. The presented vortex criteria are therefore disputable in zones with a high shear intensity. Such a case occurs at the onset of von Kármán vortices, which is manifested in Fig. 3 in the bottom structure closest to the cylinder, where no closed viscous acceleration field lines can be seen, but the vortex criteria indicate a vortex.

This simple example illustrates the ambiguity of vortex definition. Even though only the magnitude of the two composing fields is changed (orientation is fixed), the vortex criteria indicate changing shape and location of the identified vortex in the combined flow. To analyze the situation, we examine the velocity gradient tensor, which is for the present case of the following form

$$\nabla \boldsymbol{v} = \nabla \boldsymbol{v}_{\mathrm{v}} + k_{\mathrm{s}} \nabla \boldsymbol{v}_{\mathrm{s}} = \begin{bmatrix} \dfrac{\partial v_{\mathrm{v}1}}{\partial x_1} & \dfrac{\partial v_{\mathrm{v}1}}{\partial x_2} + k_{\mathrm{s}} \dfrac{\partial v_{\mathrm{s}1}}{\partial x_2} \\ -\dfrac{\partial v_{\mathrm{v}1}}{\partial x_2} & -\dfrac{\partial v_{\mathrm{v}1}}{\partial x_1} \end{bmatrix} \tag{15}$$

For zero shear, the off-diagonal velocity gradient tensor is antisymmetric, i.e., the sign of components 12 and 21 differ, but their magnitude is the same. The trace is zero from incompressibility. The shear component contributes only to element 12, and its addition can have two effects: the signs of the two components either remain opposite or become the same. In the first case, the eigenvalues remain purely imaginary and their magnitude increases with the difference between the off-diagonal components. Vortex criteria in this case indicate the presence of a vortex. In the latter case, the eigenvalues are real, and the vortex criteria indicate no vortex. Comparing the results of vortex identification with the viscous acceleration field reveals that the present vortex identification methods produce positive results in zones where viscous acceleration field lines are bent, but not closed. This suggests that, in certain cases, vortices cannot be identified properly by local methods. To obtain more relevant results, we propose to calculate the viscous acceleration field line starting from the point of interest and determine its closedness (or spiral structure in 3D).

A similar analysis was made by Elsas and Moriconi [28]. They studied also the interaction of various amounts of Lamb vortices and obtained unsatisfactory results using the swirling strength criterion when the vortices were very close to each other, the background shear was significant, or one vortex was substantially weaker than the others in its vicinity. To treat this issue, they proposed a new method. Instead of the original velocity field, they use a vector field which they denote as a pseudo-velocity field. Given the standard vorticity vector ω_i, it is defined as

$$\tilde{v}_i = \varepsilon_{ijk} \frac{\partial \omega_k}{\partial x_j} = \operatorname{curl} \boldsymbol{\omega} = \operatorname{curl}(\operatorname{curl} \boldsymbol{v}) \tag{16}$$

For an incompressible Newtonian fluid, this pseudo-velocity field is in fact proportional to the viscous acceleration field (12) since $\operatorname{curl}(\operatorname{curl} \boldsymbol{v}) = -\Delta \boldsymbol{v} = -\boldsymbol{a}_{\mu} \rho \mu^{-1}$. Then, the standard vortex identification methods can be applied to this field, but with the inclusion of a filtering function that was in the studied cases shown to eliminate most false positive zones. Assume that $\lambda_{\tilde{v},\mathrm{ci}}$ is the imaginary part of the complex eigenvalue of the gradient of the pseudo-velocity field $\tilde{\boldsymbol{v}}$. The λ_{ω}-criterion is then defined as

$$\lambda_{\omega} = H(\boldsymbol{\omega} \cdot \tilde{\boldsymbol{\omega}}) \lambda_{\tilde{v},\mathrm{ci}} \tag{17}$$

where H is the Heaviside function and $\tilde{\boldsymbol{\omega}} = \mathrm{curl}\,\tilde{\boldsymbol{v}} = -\Delta\boldsymbol{\omega}$ is related to the diffusion of vorticity. This vortex identification method indeed provided better results in the mentioned cases; however, certain false positives still appeared.

Following the idea of treating the viscous acceleration field as a pseudo-velocity field, we will now focus on its vector field lines and use them as a tool for flow topology analysis. Apart from calculating them and judging their shape, we will also investigate their geometric properties – specifically, their curvature and torsion. Let us start with the properties of vector field lines described for the case of velocity streamlines.

V. EULERIAN DEFINITION OF CURVATURE AND TORSION OF STREAMLINES

Despite their frame dependency, velocity streamlines are a widely-used post-processing tool. To obtain meaningful results, either a proper frame of reference must be chosen, or frame-independent quantities related to streamlines must be derived.

Streamline curvature has been shown to be important in turbulence modelling. In dependence on the convexity, it may substantially increase or decrease the turbulence intensity [29, 30]. In general-purpose solvers utilizing eddy-viscosity turbulence models, the streamline curvature effect is represented by Galilean-invariant quantities. For example, Spalart and Shur [31] sought a measure of whether *"the rotation of the principal axes (following a particle), and the vorticity, are in the same direction"*. Their model is used in the widespread Ansys commercial CFD software [32]. Its drawback is its complexity – it includes higher-order spatial derivatives as well as temporal derivatives. Zhang and Yang [33] proposed a simpler approach based on the Richardson number. This number is proportional to $\|\boldsymbol{\Omega}\| - \|\boldsymbol{S}\|$, which is similar to the Q-criterion (6).

If streamlines are known, their curvature and torsion can be calculated using the well-known Frenet–Serret formulas

$$\frac{\partial \boldsymbol{t}}{\partial s} = \kappa \boldsymbol{n} \tag{18}$$

$$\frac{\partial \boldsymbol{n}}{\partial s} = -\kappa \boldsymbol{t} + \tau \boldsymbol{b} \tag{19}$$

$$\frac{\partial \boldsymbol{b}}{\partial s} = -\tau \boldsymbol{n} \tag{20}$$

where s is the arclength of the streamline, $\boldsymbol{t}$ is the unit tangent vector, $\boldsymbol{n}$ is the unit normal vector, $\boldsymbol{b}$ is the unit binormal vector, κ denotes the streamline curvature, and τ stands for the streamline torsion. The three vectors $(\boldsymbol{t}, \boldsymbol{n}, \boldsymbol{b})$ form an orthogonal system. The streamline curvature is a measure of the deviation of a streamline from a straight line, and the streamline torsion is a measure of the deviation of a streamline from being planar. The streamline curvature can be computed directly from (18). Afterwards, the streamline torsion can be obtained from (19).

It is a less widely recognized fact that streamline curvature and torsion can be represented as Eulerian fields. Such a representation allows us to find zones of high streamline curvature or torsion without actually needing to calculate the streamlines. Smirnov [34] presented the derivation of the Eulerian representation of the streamline curvature. Readers interested in the step-by-step procedure are referred therein. The final relation is fairly simple

$$\frac{\partial \boldsymbol{t}}{\partial s} = \kappa \boldsymbol{n} = \mathrm{curl}\,\boldsymbol{t} \times \boldsymbol{t} = \frac{\partial t_i}{\partial x_j} t_j = T_{ij} t_j \tag{21}$$

We extend this approach by applying the same principle to (19). Considering that we are in fact calculating the directional derivative, using the corresponding formula yields

$$\frac{\partial \boldsymbol{n}}{\partial s} = \frac{\partial n_i}{\partial x_j} t_j \Rightarrow \frac{\partial \boldsymbol{n}}{\partial s} \cdot \boldsymbol{b} = \frac{\partial n_i}{\partial x_j} t_j b_i = \tau \tag{22}$$

This formula is the Eulerian representation of the streamline torsion. The unit binormal vector can be calculated simply as the cross product $\boldsymbol{t} \times \boldsymbol{n}$, where the unit tangent vector can be computed from the analysed vector field as

$$\boldsymbol{t} = \frac{\boldsymbol{v}}{\|\boldsymbol{v}\|} = \frac{v_i}{v} \tag{23}$$

and the normal vector, $\boldsymbol{n}$, can subsequently be calculated from (21).

We point out the similarity between the derivative along the streamline arclength and the convective acceleration in the Navier–Stokes equation (11). The convective acceleration in fact represents acceleration due to the velocity change along the respective streamline. Similarly, (21) represents the change of the unit tangent vector along the streamline. Plugging (23) into (21) leads to

$$\kappa n_i = \frac{1}{v^2}\left(\frac{\partial v_i}{\partial x_j} v_j - \frac{1}{v}\frac{\partial v}{\partial x_j} v_i v_j\right) \tag{24}$$

After taking the dot product of (24) with n_i and considering that $v_i n_i = 0$, we obtain

$$\kappa = \frac{1}{v^2}\frac{\partial v_i}{\partial x_j} v_j n_i \tag{25}$$

which clearly shows the connection between the convective acceleration and the streamline curvature – the streamline curvature is caused by the normal component of the convective acceleration.

Another interesting relation arises if we express the second invariant of the unit tangent vector gradient matrix T_{ij} from (21). It can be shown that it is

$$I_{2(\mathrm{T})} = \frac{1}{v^2}\left[Q + \frac{v_i}{v}\left(\frac{\partial v_j}{\partial x_i}\frac{\partial v}{\partial x_j} - \frac{\partial v_j}{\partial x_j}\frac{\partial v}{\partial x_i}\right)\right] \tag{26}$$

This reveals that the Q-criterion is related to the streamline curvature, representing the Galilean-invariant element of $I_{2(\mathrm{T})} v^2$. The remaining terms are frame-dependent. Analogously to (6), regions where the antisymmetric part of T_{ij} dominates over the symmetric part contribute positively to $I_{2(\mathrm{T})}$. Thus, local maxima can be expected in the core of zones with closed or spiral streamlines.

Plugging (24) into (22) leads, after algebraic manipulations, to the following alternative expression of the streamline torsion

$$\tau = \frac{1}{\kappa v^2}\frac{\partial}{\partial x_j}\left(\frac{\partial v_k}{\partial x_m} v_m\right) t_j b_k \tag{27}$$

This expression shows that the streamline torsion is caused by the binormal element of the derivative of the convective acceleration along the streamline. Literature dealing with the streamline torsion effects mostly considers wall-bounded flows, often in helical pipes [30, 35], but also general boundary layers and channel flows [36].

The expressions derived here for velocity streamlines are generalizable to any other vector field by simply substituting the velocity vector $\boldsymbol{v}$ with the vector field of interest. In the following, we will do this for the viscous acceleration vector field.

VI. PRACTICAL APPLICATIONS

A. Test Cases

To study the performance of methods derived from the viscous acceleration in real three-dimensional flows, we utilized data from three CFD simulations. Two of them were carried out by the authors in ANSYS Fluent (Ansys, Inc.) commercial software. For post-processing, we used ParaView 6.0, while more advanced visualizations were rendered in Blender 4.5; both are open-source software packages.

The first case represents flow around a sphere with a Reynolds number of 500. This flow was solved using a numerical model for laminar flow. The diameter of the sphere is 1 m, and the free-stream velocity is $7.3 \cdot 10^{-3}$ m·s^{-1}.

The second case is a swirl generator designed for studying swirling flow in a diffuser. This flow is turbulent, and for its modelling, the stress-blended eddy simulation (SBES) model of turbulence was chosen. It is based on blending a model based on Reynolds averaging (RANS, in this case k–ω SST) and a model based on the large eddy simulation (LES) approach. The latter is designed to resolve the turbulence cascade down to the inertial layer, providing finer details than the former model at a higher computational cost. The SBES model blends these two using a shielding function. The formulation of this shielding function is proprietary. However, at least its main goals have been published [37]. The purpose is to model the boundary layer at walls by the RANS model to avoid the associated high computational cost of the LES approach in this zone, and allow the LES approach only in the zones of strongly unsteady flow. This is a suitable compromise – details are modelled only in the zones of our interest. Various studies of flow in the present swirl generator, both numerical and experimental, have been published [15, 38–40]. The generator has two inlets – axial and tangential, allowing us to smoothly adjust the swirl intensity during operation. The resulting flow coming to the diffuser is the result of mixing of the two inflows – straight axial and swirling tangential. The snapshot used in this study features medium swirl intensity – the flow rates at both inlets are equal.

The last case is a DNS simulation of a boundary layer flow with zero pressure gradient performed at the Technical University of Madrid, discussed in [41]. DNS simulations by definition capture the whole turbulence cascade down to the smallest scales, i.e., no model of turbulence is used. The required grid resolution and number of time steps grow as a power law of the turbulent Reynolds number. For this reason, DNS is currently unfeasible for most industrial applications. Here, we used only a small portion of the whole domain in a single time instant provided by the authors as a sample field. Our subdomain consists of a portion of the wall and a limited extent of the flow domain in the normal direction. The data can be downloaded from the website (https://torroja.dmt.upm.es/turbdata/blayers/high_re/fields/, accessed on 14th December 2025). Boundary layer flow is often characterized by Reynolds number based on its momentum thickness θ. In this simulation, Re_θ ranges from 2780 to 6650. The free-stream velocity is 1 m·s^{-1}.The domain was discretized using a rectilinear grid, which was refined towards the wall in the wall-normal direction.

Computational meshes are in all three cases conformal and fully hexahedral. Their quality ranks high in common metrics, such as alignment with flow, low skewness, low aspect ratio, or smooth transitions. A mesh sensitivity study and comparison of different CFD results with experiments were performed for the swirl generator case in [15], which confirmed that the performed CFD simulations with a model of turbulence captured the flow reliably – frequency spectra and the mean velocity fields from PIV measurements were in good agreement, and similar transient phenomena of the so-called vortex rope were observed (vortex rope is a spiral vortical structure present in the diffuser, related to the vortex breakdown phenomenon – see [42–44] for reviews).

B. Vortex identification by residual vorticity magnitude

As a representative of the standard methods of vortex identification based on the velocity gradient tensor, we have chosen the residual vorticity for its elimination of shear effects, vectorial character, and magnitude with a clear physical meaning (see [38] for comparison with other methods). In Fig. 5, we present volume renderings of its magnitude field for the present test cases. We consider the volume rendering technique to be superior to the common approach using isosurfaces, since it allows for a smooth visualization of a range of values, not just one. This is achieved by an opacity transfer function, which is in this case set so that the higher the residual vorticity magnitude, the lower the opacity. Zero values are fully transparent, eliminating zones that do not belong to vortices. The opacity transfer function is denoted throughout this paper by a line in the colorbar, and it is set as linear in all the presented visualizations.

For the flow around a sphere, we can observe horseshoe vortices in the wake. Their orientation varies, i.e., the flow is asymmetric. According to the study by Li and Zhou [45], the wake is steady at Re = 200, unsteady, periodic, and symmetric at Re = 300, and unsteady, non-periodic, and fully asymmetric at Re = 400, confirming our results. The most complex flow pattern is present in the recirculation zone at the downstream half of the sphere. However, the presence of false positives attributable to bending rather than developed vortices hinders the analysis of the formation of vortices downstream of the sphere. It is notable that bending of the flow at the upstream half of the sphere leads to false positives that seem inherent to the local vortex identification methods based on the velocity gradient tensor alone.

In the swirl generator case, a vortex rope composed of intertwined vortices (darker shades of blue) can be identified within a turbulent flow, where numerous eddies are resolved by the LES approach (lighter shades of blue to white). While the vortex rope is clearly visible, the small turbulent eddies are difficult to distinguish because the visualization appears blurry. This is due to the relatively small variation of residual vorticity within these eddies. Furthermore, the projection of three-dimensional data onto a two-dimensional screen exacerbates this lack of clarity. The visual separation can be improved by reducing the opacity for the smallest values of the residual vorticity magnitude; however, the weakest vortices may then become too faint to be seen (see Appendix A). Similar results were obtained for the DNS simulation of a turbulent boundary layer. Stronger eddies in darker colors can be observed among numerous weaker eddies in lighter colors.

These difficulties are our motivation for developing enhanced methods for the visualization and analysis of vortical structures. They rely on metrics derived from the viscous acceleration field.

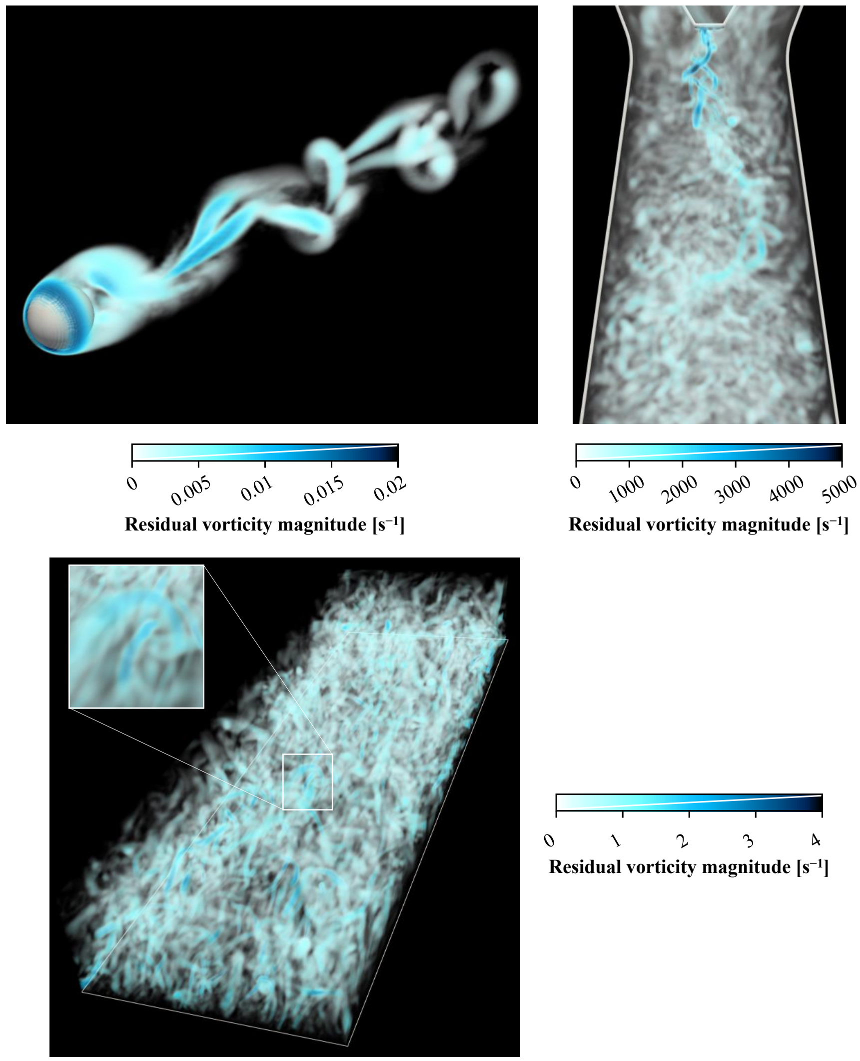

Figure 5. Volume renderings of the residual vorticity magnitude field. Top left: flow around a sphere at Re = 500, top right: turbulent swirling flow with a vortex rope in the diffuser of a swirl generator, bottom: turbulent boundary layer at a flat plate including a detailed view. White line in the colorbar represents the opacity transfer function; the opacity increases linearly from the bottom (0%) to the top (100%).

C. Enhanced methods

First, we recall the λ_ω-criterion (17) by Elsas and Moriconi. Since this criterion was proposed following the goal of reducing false positives and improving the results in cases with background shear and interacting vortices, it is naturally a promising option that could deliver better results also for our cases.

The desired effects are clearly visible when comparing the λ_ω-criterion (Fig. 6) with the residual vorticity magnitude (Fig. 5) for the flow around a sphere. The false positives close to the sphere were largely reduced; however, artifacts caused by discretization errors of higher-order spatial derivatives are visible at some locations on the sphere surface and at the boundaries of the domain decomposition, where the skewness of cells is often highest.

Especially in the swirl generator case, it can be seen that high positive values of the λ_ω-criterion are concentrated closer to the vortex core (the vortices appear thinner). The global distribution of its magnitude is very different from the residual vorticity – various structures that are hardly visible in the residual vorticity visualization are in this case among the strongest. In the downstream half, the vortex rope is practically indistinguishable from the surrounding turbulence.

In the DNS of a turbulent boundary layer, numerous structures exhibit high core magnitudes and sharp gradients, making them clearly distinguishable from the multitude of surrounding structures. Specifically, these eddies exhibit increased visual prominence, while the remaining structures lack sufficient clarity.

Images in Figs. 5 and 6 show how different visualization of the same structures can be achieved by using various identification criteria. The λ_ω-criterion values are by definition related to the magnitude of the velocity Laplacian in zones, where its vector field forms a rotational pattern. In contrast, the residual vorticity is based on the relative velocity field. From our point of view, the residual vorticity magnitude presents a better measure of the vortex intensity; therefore, we now seek suitable enhanced representations based on its field. This is where the Eulerian representation of the curvature of vector field lines comes in handy.

Neither the curvature (21), nor the torsion (22) of vector field lines alone are suitable for direct visualization. Since there can be many sources of curvature and torsion, and since their magnitude is not related to the strength of the underlying flow structures, these visualizations are rich in captured features of similar intensity, resulting in significant visual occlusion (see Appendix B). It is therefore desirable to extract only the structures of interest and add a measure of their strength. For analyses of vortical structures, this can be achieved by incorporating a vortex criterion, in our case the residual vorticity magnitude. It is zero outside of vortices, thus filtering out everything else, and its magnitude can be used as a measure of their strength since it is related to angular velocity.

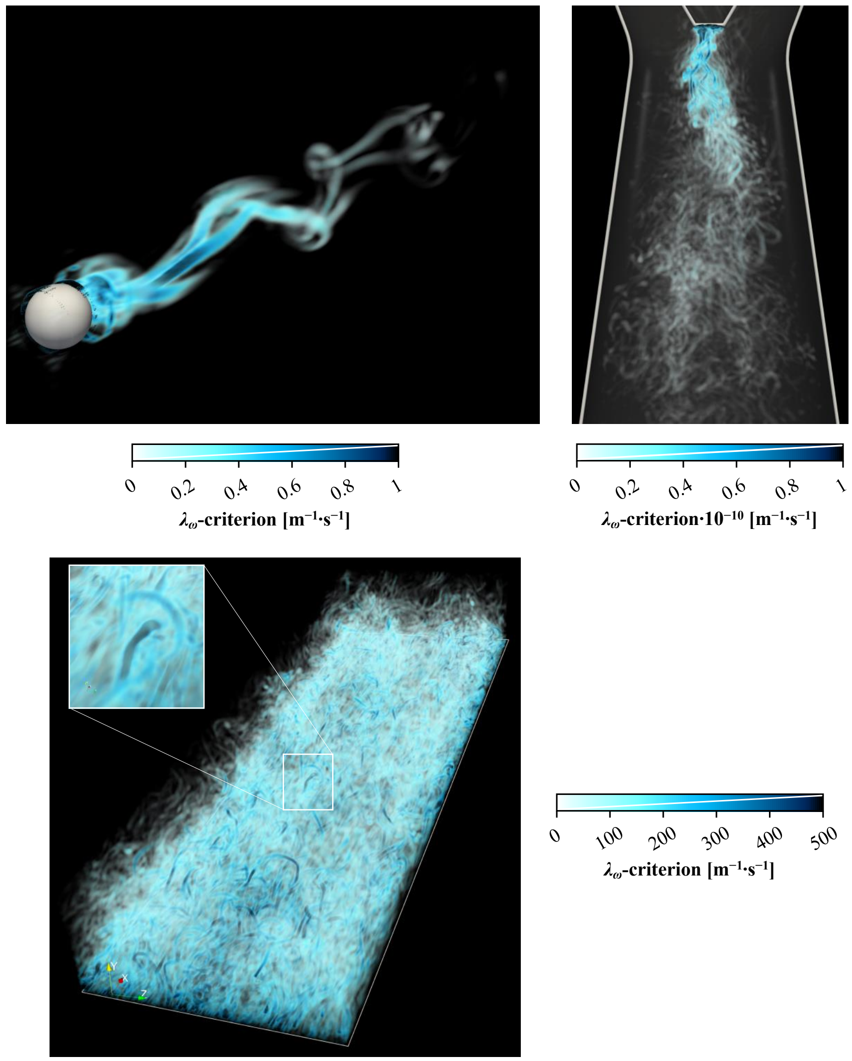

Figure 6. Volume renderings of the λ_ω-criterion field. Top left: flow around a sphere at Re = 500, top right: turbulent swirling flow with a vortex rope in the diffuser of a swirl generator, bottom: turbulent boundary layer at a flat plate including a detailed view. White line in the colorbar represents the opacity transfer function; the opacity increases linearly from the bottom (0%) to the top (100%).

Figs. 7 and 8 present volume renderings created in Blender, where color represents the curvature and torsion of the viscous acceleration field lines (hereinafter also referred to simply as curvature and torsion), and transparency is mapped to the residual vorticity magnitude. The simulation data were transferred from ParaView to Blender using the OpenVDB format, and the images were rendered using the Cycles path-tracing engine. The used combination filters out regions outside of vortical structures while preventing possible sharp transitions between removed and preserved zones. A rapid color shift from blue to lime highlights areas of peak curvature and torsion. The pictures confirm that vortices are typically associated with significant values of curvature and torsion. The torsion field is visibly affected by the inaccuracy of the discretization of higher-order derivatives (in this case fourth-order spatial derivatives of the velocity field). This fact limits its usage only to grids of a very high quality and resolution. Nevertheless, in the present cases, the visualizations still convey at least rough information about the distribution of torsion in vortical structures sufficiently larger than the mesh size. The curvature field appears less sensitive. Concentration of high values close to the vortex axis (or vortex core line) is given by the reducing radius of the associated spiral lines. Since the spiral shape is lost at the axis (unless the axis itself is spiral), we can often identify lines of low curvature in centers of vortices (since the curvature of the vortex axis is typically lower than the curvature of the surrounding spiral lines). This effect is visible in the detail of the turbulent boundary layer flow case, and it can be used for identification of vortex core lines [26]. The same holds for torsion.

The distribution and scaling of curvature led us to an idea of combining it with the residual vorticity magnitude by their multiplication. Our goal is to obtain more prominent representations of vortical structures.

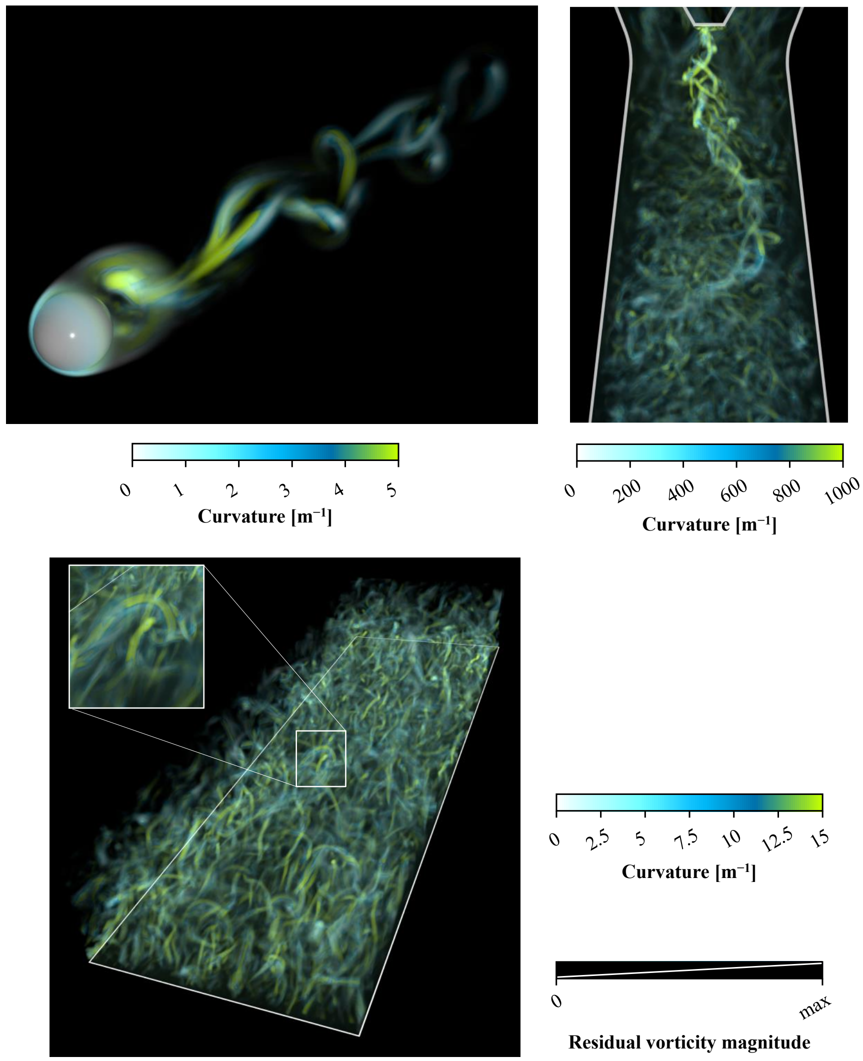

Figure 7. Volume renderings of the curvature of the viscous acceleration field lines. Colors according to the curvature values, transparency according to the residual vorticity values (ranges are the same as in Fig. 5). Top left: flow around a sphere at Re = 500, top right: turbulent swirling flow with a vortex rope in the diffuser of a swirl generator, bottom: turbulent boundary layer at a flat plate including a detailed view. White line in the bar represents the opacity transfer function; the opacity increases linearly from the bottom (0%) to the top (100%).

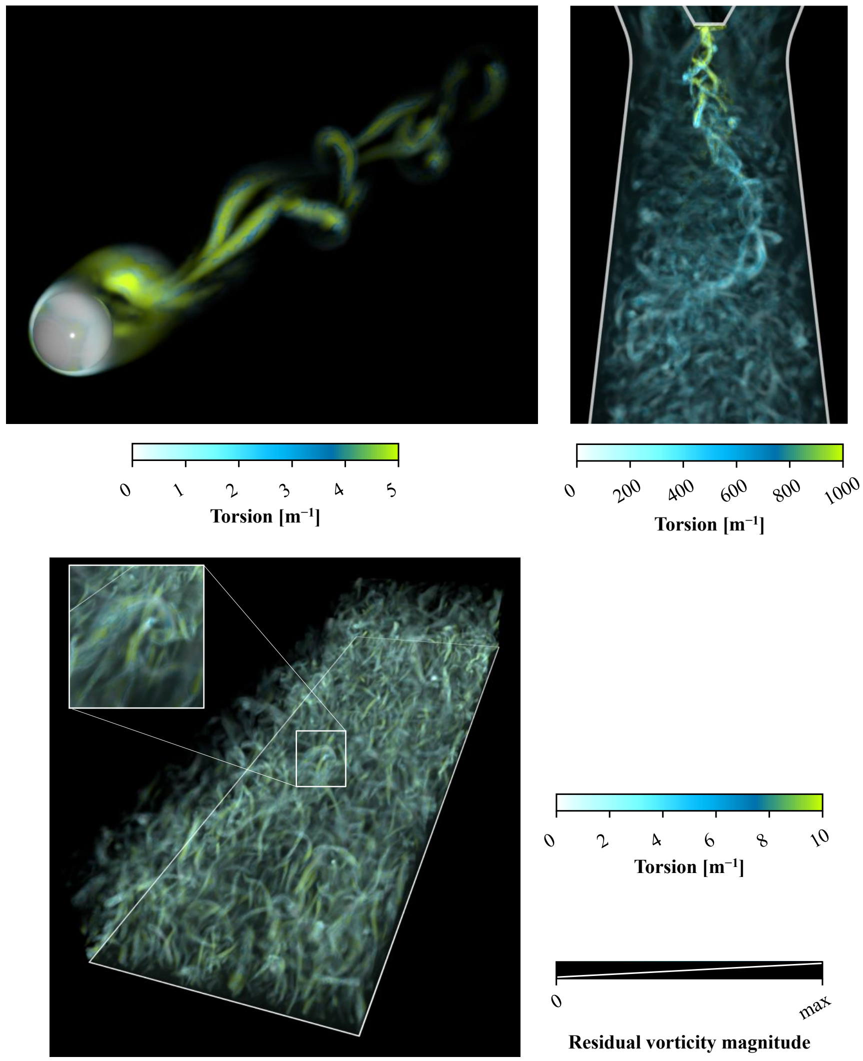

Figure 8. Volume renderings of the torsion of the viscous acceleration field lines. Colors according to the torsion values, transparency according to the residual vorticity values (ranges are the same as in Fig. 5). Top left: flow around a sphere at Re = 500, top right: turbulent swirling flow with a vortex rope in the diffuser of a swirl generator, bottom: turbulent boundary layer at a flat plate including a detailed view. White line in the bar represents the opacity transfer function; the opacity increases linearly from the bottom (0%) to the top (100%).

The intended combination of the curvature of viscous acceleration field lines and the residual vorticity magnitude is based on the following operations. The first step is to normalize each field so that reasonable visualizations are obtained for range $\langle 0{,}1 \rangle$, which is achieved by dividing the original fields by normalization constants C_1, C_2. This allows for exponentiation to arbitrary powers (m, n), as the values 0 and 1 remain unchanged. The final step is a multiplication of the two quantities. The definition of the combined variable can be written as follows

$$\kappa\omega_{\mathrm{res}}(m,n) = \left(\frac{\kappa}{C_1}\right)^m \left(\frac{\|\boldsymbol{\omega}_{res}\|}{C_2}\right)^n \tag{28}$$

To study the effect of various combinations of the powers (m, n), we have chosen the swirl generator case. Visualizations of $\kappa\omega_{\mathrm{res}}(m,n)$ for four different combinations are presented in Fig. 9. Values (0,1) correspond to the residual vorticity field in Fig. 5. Combination (0,2) hence corresponds to the residual vorticity squared. Its volume rendering visually appears more focused, making turbulent eddies surrounding the downstream part of the vortex rope more distinguishable. However, weaker structures, especially in the upstream part of the diffuser, are hardly visible (as values close to zero squared are by orders of magnitude closer to zero). A similar scaling is typical for the Q-criterion, which is also proportional to the square of the velocity derivatives. Combination (1,1) yielded a more focused representation while preserving the visibility of weaker structures. This is due to the fact that curvature depends solely on the structure geometry, and it is invariant to flow strength metrics (e.g., angular velocity or rate of diffusion). Consequently, peak values are often comparable in both weak eddies and strong coherent structures. The concentration of high values close to the vortex core lines followed by a sharp decay beyond a certain border is responsible for highlighting the central zones of vortices. At the same time, this suppresses the surrounding zones (still considered part of the vortex by residual vorticity), which typically cause visualizations to appear blurry. Increasing the power m related to the curvature field to 2 magnifies the described effects; however, numerical artifacts at the diffuser wall become more apparent.

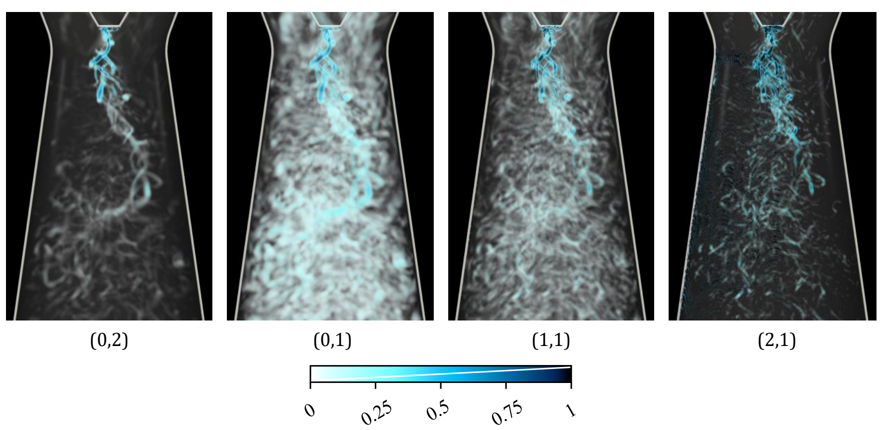

Figure 9. Volume renderings of $\kappa\omega_{\mathrm{res}}(m,n)$ from (28) for the swirl generator case for various values of (m,n) given below each picture. White line in the colorbar represents the opacity transfer function; the opacity increases linearly from the bottom (0%) to the top (100%).

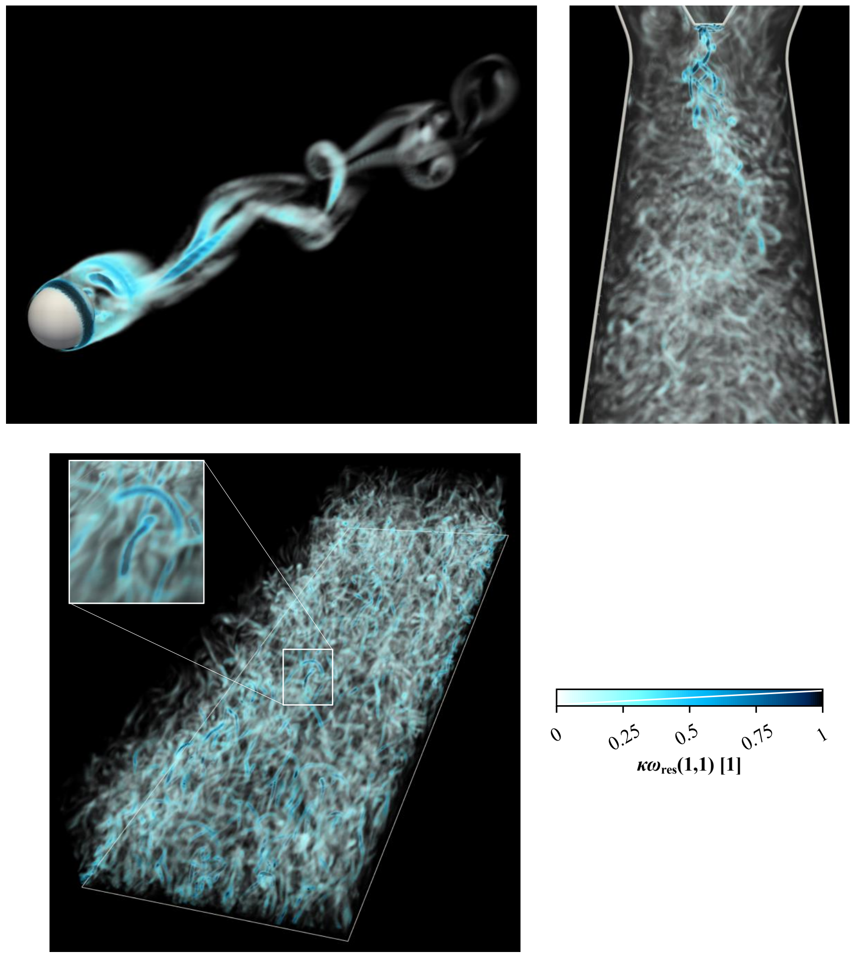

Figure 10. Volume renderings of $\kappa\omega_{\mathrm{res}}(1{,}1)$ from (28). Top left: flow around a sphere at Re = 500, top right: turbulent swirling flow with a vortex rope in the diffuser of a swirl generator, bottom: turbulent boundary layer at a flat plate including a detailed view. White line in the colorbar represents the opacity transfer function; the opacity increases linearly from the bottom (0%) to the top (100%).

Based on the presented results for the swirl generator case, we consider $\kappa\omega_{\mathrm{res}}(1{,}1)$ to be a well-balanced combination of curvature and residual vorticity. It yields enhanced representations of vortical structures, where small turbulent eddies are more easily distinguishable from one another compared to pure residual vorticity visualizations. Furthermore, the magnitude distribution ensures that weak structures remain clearly visible. In Fig. 10, this combination is also visualized for the other two cases, where the same effects can be observed. These benefits are particularly evident in turbulent flow cases, which are characterized by a myriad of small-scale eddies. The combination of residual vorticity and the curvature of the viscous acceleration field lines, therefore, appears to be a suitable method for post-processing scale-resolving CFD simulations of turbulent flow.

Visualization of viscous acceleration field lines (or, equivalently, streamlines of $\tilde{\boldsymbol{v}}$) can also be a useful tool for flow topology studies. If we are interested in vortical structures, the fields of $\kappa\omega_{\mathrm{res}}(m,n)$ or simply ω_{res} can be used to find suitable initial points for these lines by clipping the domain to zones where these quantities are positive. Example visualizations for the flow around a sphere and the turbulent boundary layer at a flat plate (only a subzone corresponding to the detailed view from the previous figures is used) are in Fig. 11. It is apparent that viscous acceleration lines are of spiral shape within prominent vortex structures manifested by high values of the residual vorticity. One application of these representations is to qualitatively study properties such as the orbital compactness or cylindricity of vortices (in [46] defined quantitatively based on the velocity gradient properties). Another use is for distinguishing true vortices (exhibiting spiral or closed patterns) from false positives in ω_{res} caused by bending (e.g., near the upstream half of the sphere in the first case).

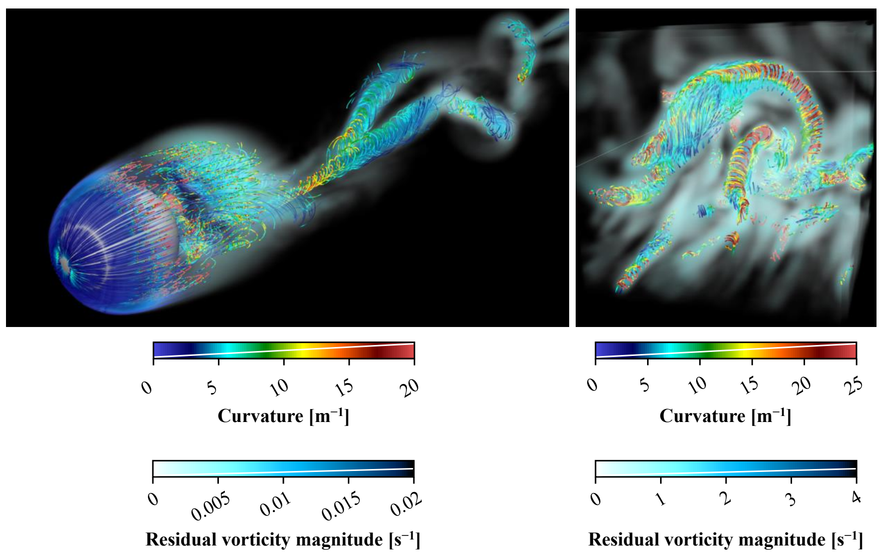

Figure 11. Field lines of the viscous acceleration $\boldsymbol{a}_{\mu}$ (or, equivalently, streamlines of $\tilde{\boldsymbol{v}}$) initialized in points with positive residual vorticity magnitude. Left: flow around a sphere at Re = 500, right: turbulent boundary layer at a flat plate (subzone from the detailed view from previous figures). Colors represent their curvature (for comparison, the radius of the sphere is 0.5 m, corresponding to a curvature of 2 m^{-1}). Spiral patterns within vortices are clearly visible, allowing for a qualitative evaluation of properties such as their orbital compactness or cylindricity.

VII. CONCLUSION

This work has shown that the viscous acceleration vector field can be utilized for fine visualizations of vortical structures, in addition to classical approaches based on the velocity gradient tensor. The objectivity of this field makes its field lines (analogy to streamlines) also objective. The patterns of these lines were shown to be suitable for qualitative analyses of flow structures. They inform us how the viscous acceleration shapes the flow.

We combined the Eulerian representation of the curvature of viscous acceleration field lines with a vortex criterion (the residual vorticity magnitude) to achieve new representations of vortical structures. The calculation of this quantity is straightforward – it is computed locally at a given time instant, which makes it practical for everyday engineering use. The most complex operation is the calculation of third-order spatial derivatives, which may render the results to be distorted on poor-quality meshes (see Appendix C for examples). Another disadvantage, resulting from the local property, is the presence of false positives connected with bending rather than vortices. Also, the user should keep in mind that residual vorticity is only Galilean-invariant, which makes the outcomes sensitive to a frame rotation. Despite these difficulties, the presented results for three CFD simulations (flow around a sphere at Re = 500, turbulent swirling flow with a vortex rope in the diffuser of a swirl generator, and a DNS of a turbulent boundary layer at a flat plate) were found to be meaningful. Notably, the visualizations created by volume rendering led to an enhanced representation of the captured vortices, with a stronger focus on their central zones. This property significantly improved the distinguishability of turbulent eddies compared to the visualization of the raw residual vorticity magnitude, rendering the proposed method a strong candidate for post-processing scale-resolving CFD simulations of turbulent flows. Methods based on the viscous acceleration vector field are particularly relevant for cases where energy losses generated by flow structures are of interest (see e.g. [47–49]).

Correct identification of vortical structures still remains an open research topic. We believe that rigorous methods aimed at meeting all requirements [6] must be based on careful analysis of particle trajectories, making them computationally expensive and, therefore, unsuitable for everyday engineering use. This justifies further development of simpler methods like those presented in this paper. The goals for future research should be to develop both a rigorous vortex identification method widely accepted by the community, and a simple proxy for everyday engineering use supported by comparative studies identifying limitations such as sources of false positives. We consider methods based on the viscous acceleration to be a strong candidate for the latter, particularly for its objectivity and tangential nature with respect to the relevant flow pattern.

ACKNOWLEDGMENT

The authors gratefully acknowledge the Czech Science Foundation for funding the project *Vortical structures: advanced identification and efficient numerical simulation* number 23-06159S, which was used to carry out this work. We also thank our colleague, prof. Pavel Rudolf, for reviewing the draft version of this paper and providing valuable feedback.

AUTHOR DECLARATIONS

Conflict of Interest

The authors have no conflict to disclose.

Author Contributions

Ondřej Urban: conceptualization (equal), investigation (equal), methodology (equal), software (lead), validation (lead), visualization (lead), writing – original draft (lead). **František Pochylý:** conceptualization (equal), investigation (equal), formal analysis (lead), methodology (equal), writing – review & editing (equal). **Jakub Šístek:** investigation (equal), writing – review & editing (equal), project administration (equal), funding acquisition (equal). **Marek Pátý:** conceptualization (equal), investigation (equal), writing – review & editing (equal). **David Štefan:** investigation (equal), writing – review & editing (equal), project administration (equal), funding acquisition (equal).

DATA AVAILABILITY

The data that support the findings of this study are available from the corresponding author upon reasonable request.

APPENDIX A: INFLUENCE OF THE OPACITY TRANSFER FUNCTION ON VOLUME RENDERINGS

This appendix illustrates how the resulting volume renderings—specifically those of the residual vorticity magnitude for the swirl generator case—are influenced by the configuration of the opacity transfer function. Fig. 12 contains three volume renderings with various opacity transfer functions. The left image corresponds to that in Fig. 5. The opacity transfer function is linear from 0 to the maximum value of 5000 s^{-1}. Anything above this limit is fully opaque. With this setting, the turbulent eddies appear blurry. Increasing the bottom limit to 250 s^{-1} (anything below this value is fully transparent) substantially improved the visual separation for the price of losing the structures that fall below this limit. Using a nonlinear opacity transfer function in the range from 0 to 1000 s^{-1} with a lower initial growth rate, further increasing linearly to the upper limit, preserved the weakest structures while maintaining improved visual separation of stronger vortices. However, the weakest structures still appear blurry and, moreover, relatively faint.

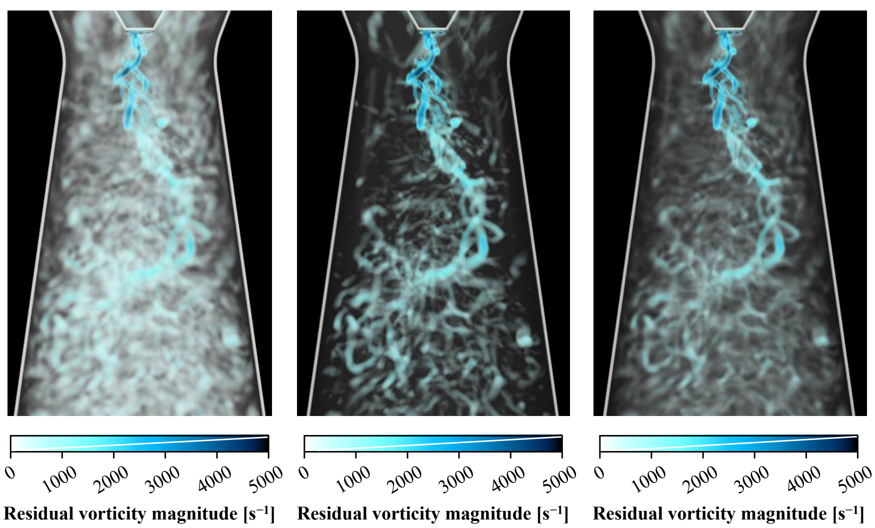

Figure 12. Volume renderings of the residual vorticity magnitude field for turbulent swirling flow with a vortex rope in the diffuser of a swirl generator. Left: linear opacity transfer function from 0 to 5000 s^{-1}, center: linear opacity transfer function from 250 to 5000 s^{-1}, right: nonlinear opacity transfer function from 0 to 1000 s^{-1} with a lower initial growth rate continued linearly to 5000 s^{-1}.

APPENDIX B: VISUALIZATIONS OF THE CURVATURE AND TORSION OF VISCOUS ACCELERATION FIELD LINES

This appendix shows that Eulerian fields of the curvature and torsion of vector field lines (be it a suitable velocity field or viscous acceleration) are usually too rich in features. Figure 13 displays volume renderings of the curvature and torsion of viscous acceleration field lines for the DNS of a turbulent boundary layer. The density of structures makes it impossible to see through the domain; therefore, filtering or clipping to specific zones of interest is needed.

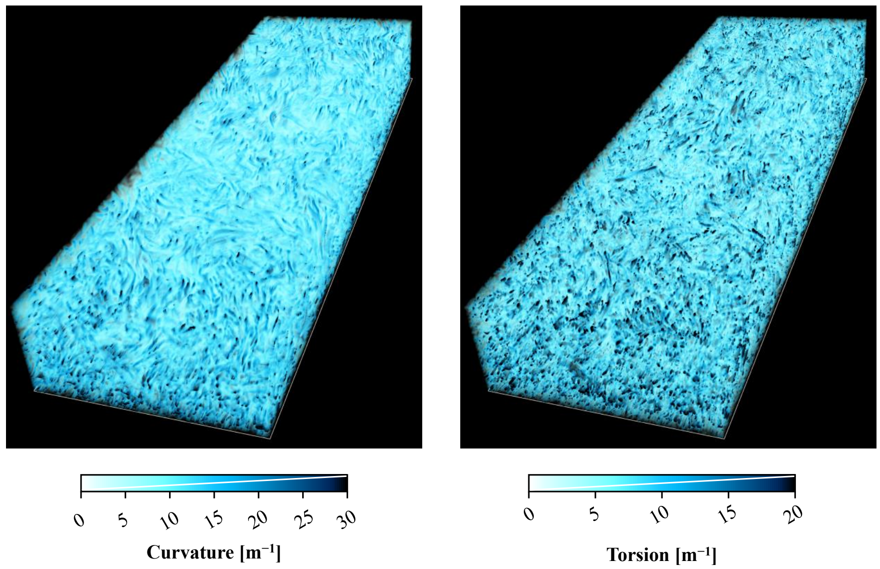

Figure 13. Volume renderings of the curvature and torsion of viscous acceleration field lines for the DNS of a turbulent boundary layer at a flat plate.

APPENDIX C: LIMITATIONS

This appendix presents two examples, where insufficient mesh quality, the primary limitation of viscous acceleration-based methods, introduced numerical artifacts.

The first example, Fig. 14, is a flow around a sphere at Re = 300 (the sphere diameter is 1 m and the inflow velocity is 1 m·s^{-1}). The wake is in this case symmetric and exhibits similar vortices to those obtained for Re = 500. The domain is cylindrical and discretized using a fully conformal hexahedral grid. However, the central part of the grid was created by transforming rectilinear grid to a cylindrical shape, which causes the cells from the original corners to be highly skewed after the transformation. This caused numerical artifacts in the visualization of $\kappa\omega_{\mathrm{res}}(1,1)$.

The second example, Fig. 15, is a centrifugal pump operating in turbine mode. The rotational speed is 1000 rpm, the diameter of the pump inlet pipe (which is in turbine mode actually outlet pipe) is 80 mm, and the mean axial velocity in the pipe is 4.5 m·s^{-1}. More information can be found in [50]. The flow is turbulent, simulated using the scale-resolving SBES model of turbulence. In this setting, we encounter swirling flow within the pipe, with a direction of rotation opposite to that of the impeller. The visualization of the residual vorticity magnitude reveals a large strong vortex fixed to the central hub. Similarly to the previous case, the visualization of $\kappa\omega_{\mathrm{res}}(1,1)$ is affected by numerical artifacts. In this case, however, these are caused by cells with a high aspect ratio originating in the hub boundary layer, which are propagated downstream to maintain mesh conformality. At the boundary of the domain decomposition, there is a big difference in the size of neighboring cells, which is also not desirable. An interesting finding is that the viscous acceleration field contains a relatively thin ring with a significantly higher magnitude. This ring represents a boundary between the large vortex structure and the outer flow. Moreover, the large vortex structure apparently contains smaller internal structures. However, to properly resolve such fine details, a more uniform, refined mesh is desirable.

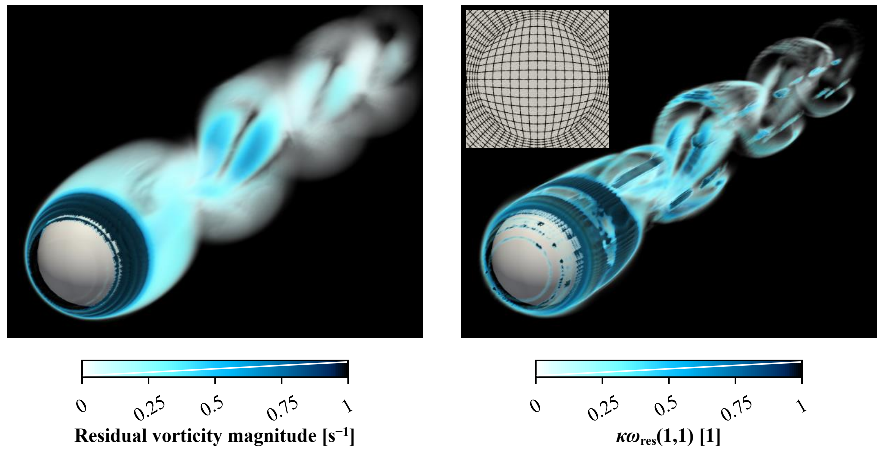

Figure 14. Volume renderings of the residual vorticity magnitude and $\kappa\omega_{\text{res}}(1,1)$ for a flow around a sphere at Re = 300. Numerical artifacts caused by highly skewed cells are apparent in the right picture. A slice through the mesh is also shown.

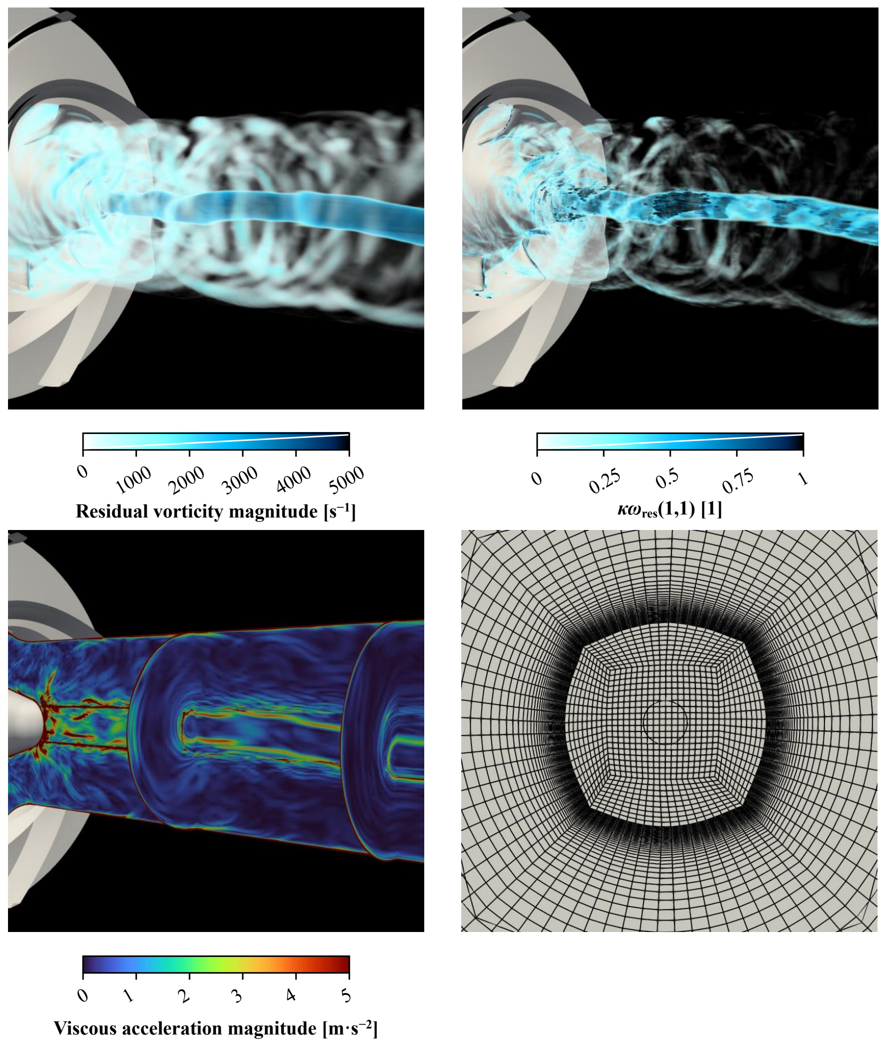

Figure 15. A centrifugal pump operating in turbine mode. Top: volume renderings of the residual vorticity magnitude and $\kappa\omega_{\mathrm{res}}(1,1)$, bottom: visualization of viscous acceleration magnitude in several planes and a slice through the mesh of the pipe. Numerical artifacts are apparent in the visualizations of $\kappa\omega_{\mathrm{res}}(1,1)$ and the viscous acceleration magnitude.

REFERENCES

[1] A. Colagrossi, S. Marrone, P. Colagrossi, and D. Le Touzé, "Da Vinci's observation of turbulence: A French-Italian study aiming at numerically reproducing the physics behind one of his drawings, 500 years later" Physics of Fluids **33**, 115122 (2021). DOI: 10.1063/5.0070984.

[2] M. Van Dyke, *An Album of Fluid Motion* (The Parabolic Press, Stanford, United States of America, 1988).

[3] J. C. R. Hunt, A. A. Wray, and P. Moin, "Eddies, streams, and convergence zones in turbulent flows," in *Center for turbulence research report CTR-S88* (2005, 193–208).

[4] G. Jeong, and F. Hussain, "On the identification of a vortex," Journal of Fluid Mechanics **285**, 69–94 (1995). DOI: 10.1017/S0022112095000462.

[5] J. Zhou, R. J. Adrian, S. Balachandar, and T. M. Kendall, "Mechanisms for generating coherent packets of hairpin vortices in channel flow," Journal of Fluid Mechanics **387**, 353–396 (1999). DOI: 10.1017/S002211209900467X.

[6] V. Kolář, "Vortex identification: New requirements and limitations," International Journal of Heat and Fluid Flow **28**(4), 638–652 (2007). DOI: 10.1016/j.ijheatfluidflow.2007.03.004.

[7] C. Liu, Y. Gao, S. Tian, and X. Dong, "Rortex—A new vortex vector definition and vorticity tensor and vector decompositions," Physics of Fluids **30**, 035103 (2018). DOI: 10.1063/1.5023001.

[8] B. P. Epps. "Review of Vortex Identification Methods," in *55th AIAA Aerospace Sciences Meeting* (American Institute of Aeronautics and Astronautics, United States of America, 2017). DOI: 10.2514/6.2017-0989.

[9] P. Chakraborty, S. Balachandar, and R. J. Adrian, "On the relationships between local vortex identification schemes," Journal of Fluid Mechanics **535**, 189–214 (2005). DOI: 10.1017/S0022112005004726.

[10] D. Drikakis, and P. K. Smolarkiewicz, "On Spurious Vortical Structures," Journal of Computational Physics **172**(1), 309–325 (2001). DOI: 10.1006/jcph.2001.6825.

[11] S. Ghosal, "An Analysis of Numerical Errors in Large-Eddy Simulations of Turbulence," Journal of Computational Physics **125**(1), 187–206 (1996). DOI: 10.1006/jcph.1996.0088.

[12] G. Haller, "An Objective Definition of a Vortex," Journal of Fluid Mechanics **525**, 1–26 (2005). DOI: 10.1017/S0022112004002526.

[13] M. S. Chong, A. E. Perry, and B. J. Cantwell, "A general classification of three-dimensional flow fields," Physics of Fluids A: Fluid Dynamics **2**(5), 765–777 (1990). DOI: 10.1063/1.857730.

[14] P. Chakraborty, S. Balachandar, and R. J. Adrian, "On the relationships between local vortex identification schemes," Journal of Fluid Mechanics **535**, 189–214 (2005). DOI: 10.1017/S0022112005004726.

[15] O. Urban, "Reduced-order Model of Swirling Flow," Doctoral thesis (Brno University of Technology, Brno, the Czech Republic, 2022).

[16] M. Pátý, and S. Lavagnoli, "A Novel Vortex Identification Technique Applied to the 3D Flow Field of a High-Pressure Turbine," Journal of Turbomachinery **142**(3), 031004 (2020). DOI: 10.1115/1.4045471.

[17] O. Urban, M. Kurková, and F. Pochylý, "Mitigation of swirling flow with a vortex rope by passive installations—Theory, simulations, and experiments," Physics of Fluids **34**, 124111 (2022). DOI: 10.1063/5.0128029.

[18] C. Levit, and T. Lasinski. "A tool for visualizing the topology of three-dimensional vector fields," in *Proceeding Visualization '91* (IEEE, San Diego, 1991), pp. 33–40. ISBN 0-8186-2245-8.

[19] X. Qu, R. He, and T. Wang, "Vortex Identification Method Based on Topological Analysis and Velocity Gradient Invariance," Journal of Fluids Engineering **146**(7), 071111 (2024). DOI: 10.1115/1.4065293.

[20] H. Bhatia, G. Norgard, V. Pascucci, and P. T. Bremer, "The Helmholtz-Hodge Decomposition - A Survey," IEEE Transactions on Visualization and Computer Graphics **19**(8), 1386–1404 (2013). DOI: 10.1109/TVCG.2012.316.

[21] A. Wiebel, C. Garth, and G. Scheuermann, "Computation of Localized Flow for Steady and Unsteady Vector Fields and Its Applications," IEEE Transactions on Visualization and Computer Graphics **13**(4), 641–651 (2007). DOI: 10.1109/TVCG.2007.4293009.

[22] T. Günther, M. Gross, and H. Theisel, "Generic objective vortices for flow visualization," ACM Transactions on Graphics **36**(4), 141 (2017). DOI: 10.1145/3072959.3073684.

[23] T. Günther, and H. Theisel, "Hyper-Objective Vortices," IEEE Transactions on Visualization and Computer Graphics **26**(3), 1532–1547 (2018). DOI: 10.1109/TVCG.2018.2868760.

[24] Y. Levy, D. Degani, and A. Seginer, "Graphical visualization of vortical flows by means of helicity," AIAA Journal **28**(8), 1347–1352 (1990). DOI: 10.2514/3.25224.

[25] D. Sujudi, and R. Haimes, "Identification of swirling flow in 3-D vector fields," 12th AIAA CFD Conference, San Diego CA (1995). DOI: 10.2514/6.1995-1715.

[26] M. Roth, and R. Peikert, "A Higher-Order Method For Finding Vortex Core Lines," in *Proceedings Visualization '98* (IEEE, United States of America, 1998). DOI: 10.1109/VISUAL.1998.745296.

[27] H. Xu, X. Cai, and C. Liu, "Liutex (vortex) core definition and automatic identification for turbulence vortex structures," Journal of Hydrodynamics **31**, 857–863 (2019). DOI: 10.1007/s42241-019-0066-5.

[28] J. H. Elsas, L. Moriconi, "Vortex identification from local properties of the vorticity field," Physics of Fluids **29**, 015101 (2017). DOI: 10.1063/1.4973243.

[29] M. M. Gibson. Effects of Streamline Curvature on Turbulence. In: Frontiers in Fluid Mechanics (Berlin, Springer, 1985, 184–198). ISBN 978-3-642-46545-1.

[30] T. J. Hüttl, and R. Friedrich, "Influence of curvature and torsion on turbulent flow in helically coiled pipes," International Journal of Heat and Fluid Flow **21**(3), 345–353 (2000). DOI: 10.1016/S0142-727X(00)00019-9.

[31] P. R. Spalart, and M. Shur, "On the sensitization of turbulence models to rotation and curvature," Aerospace Science and Technology **1**(5), 297–302 (1997). DOI: 10.1016/S1270-9638(97)90051-1.

[32] ANSYS, Inc., ANSYS CFX-Solver Theory Guide, Release 2022 R2 (ANSYS, Inc., Canonsburg, PA, 2022).

[33] Q. Zhang, and Y. Yang, "A new simpler rotation/curvature correction method for Spalart–Allmaras turbulence model," Chinese Journal of Aeronautics **26**(2), 326–333 (2013). DOI: 10.1016/j.cja.2013.02.009.

[34] V. I. Smirnov, *A Course of Higher Mathematics Volume II: Advanced Calculus* (Pergamon Press, Great Britain, 1964).

[35] M. R. H. Nobari, and A. Malvandi, "Torsion and curvature effects on fluid flow in helical annulus," International Journal of Non-Linear Mechanics **57**, 90–101 (2013). DOI: 10.1016/j.ijnonlinmec.2013.06.014.

[36] R. Perven, J. Philip, and J. Klewicki, "Statistical properties of streamline geometry in turbulent wall-flows," Physical Review Fluids **6**, 034609 (2021). DOI: 10.1103/PhysRevFluids.6.034609.

[37] F. Menter. "Stress-Blended Eddy Simulation (SBES)—A New Paradigm in Hybrid RANS-LES Modeling," in *Progress in Hybrid RANS-LES Modelling* (Springer, Cham, 2016). ISBN 978-3-319-70030-4.

[38] O. Urban, M. Kurková, and P. Rudolf, "Application of Computer Graphics Flow Visualization Methods in Vortex Rope Investigations," Energies **14**(3), 623 (2021). DOI: 10.3390/en14030623.

[39] D. Štefan, P. Rudolf, M. Hudec, V. Uruba, P. Procházka, and O. Urban, "Experimental investigation of vortex ring formation as a consequence of spiral vortex re-connection," IOP Conference Series: Earth and Environmental Science **405**, 012033 (2019).

[40] D. Štefan, M. Hudec, V. Uruba, P. Procházka, O. Urban, and P. Rudolf, "Experimental investigation of swirl number influence on spiral vortex structure dynamics," IOP Conference Series: Earth and Environmental Science **774**, 012085 (2021).

[41] J. A. Sillero, J. Jiménez, and R. D. Moser. "One-point statistics for turbulent wall-bounded flows at Reynolds numbers up to $\delta+ \approx 2000$," Physics of Fluids **25**, 105102 (2013). DOI: 10.1063/1.4823831.

[42] M. Escudier. "Vortex breakdown: Observations and explanations," Progress in Aerospace Sciences **25**(2), 189–229 (1988). DOI: 10.1016/0376-0421(88)90007-3.

[43] O. Lucca-Negro, and T. O'Doherty. "Vortex breakdown: a review," Progress in Energy and Combustion Science **27**(4), 431–481 (2001). DOI: 10.1016/S0360-1285(00)00022-8.

[44] M. G. Hall. "Vortex breakdown," Annual Review of Fluid Mechanics **4**(1), 195–218 (1972). DOI: 0.1146/annurev.fl.04.010172.001211.

[45] J. Li, and B. Zhou, "The Symmetry and Stability of the Flow Separation around a Sphere at Low and Moderate Reynolds Numbers," Symmetry **13**(12), 2286 (2021). DOI: 10.3390/sym13122286.

[46] V. Kolář, and J. Šístek, "Two complementary eigen-based geometric properties of a vortex," Physics of Fluids **36**, 111703 (2024). DOI: 10.1063/5.0238534.

[47] D. You, M. Wang, P. Moin, and R. Mittal, "Large-eddy simulation analysis of mechanisms for viscous losses in a turbomachinery tip-clearance flow," Journal of Fluid Mechanics **586**, 177–204 (2007). DOI: 10.1017/S0022112007006842.

[48] L. Zemanová, "Disc Friction Loss in Centrifugal Pumps and Hydraulic Turbines," Doctoral thesis (Brno University of Technology, Brno, the Czech Republic, 2022).

[49] B. Luo, J. Zhang, F. Cheng, and Y. Liu, "Numerical simulation of evolution pattern of vortices in Taylor–Couette flow with three-lobe multiwedge clearance," Physics of Fluids **36**, 064107 (2024). DOI: 10.1063/5.0207438.

[50] D. Štefan, M. Hudec, V. Habán, and F. Pochylý, "Experimental Study on Hysteresis during Cavitating Vortex Onset in Pump-as-Turbine Applications," IOP Conference Series: Earth and Environmental Science **1561**, 012017 (2025).